



Contents lists available at ScienceDirect

Journal of Industrial and Engineering Chemistry

journal homepage: www.elsevier.com/locate/jiec



Numerical evaluation on the intraparticle transfer in butylene oxidative dehydrogenation fixed-bed reactor over ferrite catalysts

Kai Huang^{a,*}, Sheng Lin^a, Jiejie Wang^a, Zhenghong Luo^{b,*}

^aSchool of Chemistry and Chemical Engineering, Southeast University, Nanjing 211189, PR China

^bDepartment of Chemical Engineering, School of Chemistry and Chemical Engineering, Shanghai Jiao Tong University, Shanghai 200240, PR China

ARTICLE INFO

Article history:

Received 15 December 2014

Received in revised form 15 March 2015

Accepted 7 April 2015

Available online xxx

Keywords:

Oxidative dehydrogenation

Fixed bed

Single particle model

Mathematical modeling

Hydrodynamics

Porous medium model

ABSTRACT

Ferrite catalysts with high intraparticle pore volume and surface area are frequently used in the oxidative dehydrogenation of butylene. Whether the non-inclusion of intraparticle transfer limitation in fixed-bed reactors for oxidative dehydrogenation over ferrite catalysts in previous studies is appropriate remains unclear. In this study, we attempt to verify this process using a multi-scale modeling technology. The multi-scale model consists of a porous medium model and a single particle model under the oxidative dehydrogenation condition. This model can predict the influences of intraparticle transfer on the main component distributions in reactors and demonstrate that the intraparticle transfer limitation is obvious.

© 2015 The Korean Society of Industrial and Engineering Chemistry. Published by Elsevier B.V. All rights reserved.

Introduction

Intraparticle molecule diffusion and heat transfer should be involved in gas–solid multi-phase catalytic reactors because reactions occur at the active sites of catalyst particles [1]. A multi-scale structure (i.e., single catalyst particles, particle clusters/bubbles, and reactor scale) and multi-scale phenomenon (i.e., hydrodynamics, heat and mass transfer, and catalytic reaction kinetics) exist in this reaction process [2]. Therefore, these factors should be considered when gas–solid catalytic reaction occurs in a reactor.

The multi-scale phenomenon in reactors has recently attracted much attention [1], and various teams have developed multi-scale reactor models to describe the multi-scale phenomenon in gas–solid multi-phase catalytic reactors. Li et al. [3] developed the energy minimization multi-scale (EMMS) model for particle–fluid flow in gas–solid fluidized bed reactors (FBRs). The EMMS model was subsequently modified as an analytical multi-scale method to elucidate its principles [4–6]. Wang et al. [7,8] suggested a multi-scale CFD model to describe the gas–solid flows in FBRs for FCC. Yang et al. [9] constructed a multi-scale model that considered the heat transfer, mass transfer, momentum transfer, and fluid flow

with reactions at different spatiotemporal scales for the riser reactor of secondary reactions of fluid catalytic cracking gasoline. Dompazis et al. [10] developed a comprehensive multi-scale, multi-phase, and multi-compartment dynamic model to analyze the extent of particle segregation in the catalysis in gas-phase ethylene-propylene copolymerization FBRs. Andersson et al. [11] presented a multi-scale simulation method for modeling dispersions in a novel multiphase reactor, which is a continuous reactor that consists of repeated identical small mixing elements. Ghouse et al. [12] developed a multi-scale, dynamic, two-dimensional, and heterogeneous model for catalytic methane reforming. Chen et al. [13] developed a multi-scale CFD model based on a direct concurrent multi-scale approach. This technique incorporates a single particle model (SPM) and a two-phase CFD model to predict the effects of intraparticle transfer in the flow field and main composition distributions of a catalytic reaction that converts methanol to olefins in an FBR. Based on a similar approach, Zhu et al. [14] developed a multi-scale CFD model to describe the flow behavior and catalytic hydrogenation of dimethyl oxalate in an FBR. To model fixed-bed thermo-chemical processes of biomass as a multi-scale problem, Anca-Couce et al. [15] presented a multi-scale model considering the molecule, particle, and reactor levels. A framework for a multi-scale model for dynamic fixed-bed/moving-bed thermo-chemical conversion processes and the respective numerical solution method were introduced in their work. However, this model was not built based on the CFD

* Corresponding authors. Tel.: +86 25 52090623; fax: +86 21 54745602.

E-mail addresses: huangk@seu.edu.cn (K. Huang), luozh@sjtu.edu.cn (Z. Luo).

<http://dx.doi.org/10.1016/j.jiec.2015.04.001>

1226-086X/© 2015 The Korean Society of Industrial and Engineering Chemistry. Published by Elsevier B.V. All rights reserved.

Nomenclature

A_i	kinetic parameter of the i th step, $\text{mol} \cdot \text{kg}(\text{catalyst})^{-1} \cdot \text{h}^{-1} \cdot \text{Pa}^{-1}$
B	permeability factor
$C_{p_{cat}}$	mass heat capacity of catalyst, $\text{kJ} \cdot \text{kg}^{-1} \cdot \text{K}^{-1}$
C_{p_i}	mass heat capacity of i component, $\text{kJ} \cdot \text{kg}^{-1} \cdot \text{K}^{-1}$
d_0	catalyst average diameter, m
$D_{i,eff}$	effective diffusion coefficient of the i th component, $\text{m}^2 \cdot \text{s}^{-1}$
D_{im}	Fick diffusion coefficient of the i th component, $\text{m}^2 \cdot \text{s}^{-1}$
D_{ik}	Knudsen diffusion coefficient of the i th component, $\text{m}^2 \cdot \text{s}^{-1}$
E_g	total fluid energy, $\text{kg} \cdot \text{m}^2 \cdot \text{s}^{-2}$
E_s	total solid medium energy, $\text{kg} \cdot \text{m}^2 \cdot \text{s}^{-2}$
f	Fanning coefficient
g	gravitational acceleration, $\text{m}^2 \cdot \text{s}^{-1}$
$h_{i,g}$	heat transfer coefficient, $\text{W} \cdot \text{m}^{-2} \cdot \text{K}^{-1}$
H_i	enthalpy of the i th component, $\text{kJ} \cdot \text{kg}^{-1}$
h_i	species enthalpy of formation, $\text{kJ} \cdot \text{kg}^{-1}$
\bar{I}	identity matrix
$J_{i,r}$	mass diffusion flux, $\text{kg} \cdot \text{m}^2 \cdot \text{s}^{-2}$
\bar{J}_i	diffusion flux of species i , $\text{kg} \cdot \text{m}^2 \cdot \text{s}^{-2}$
$k_{i,g}$	mass transfer coefficient, $\text{m}^2 \cdot \text{s}^{-1}$
k_i	intrinsic rate constant of the i th step based on species mass fraction, $\text{mol} \cdot \text{kg}(\text{catalyst})^{-1} \cdot \text{h}^{-1} \cdot \text{Pa}^{-1}$
k_f	fluid phase thermal conductivity, $\text{W} \cdot \text{s}^{-1} \cdot \text{K}^{-1}$
k_s	solid medium thermal conductivity, $\text{W} \cdot \text{s}^{-1} \cdot \text{K}^{-1}$
k_{eff}	effective thermal conductivity of the medium, $\text{W} \cdot \text{s}^{-1} \cdot \text{K}^{-1}$
M	mixture fluid molar mass, $\text{kg} \cdot \text{kmol}^{-1}$
M_i	molar mass of the i th component, $\text{kg} \cdot \text{kmol}^{-1}$
M_0	mixture fluid molar mass at bulk, $\text{kg} \cdot \text{kmol}^{-1}$
N_r	number of chemical species
p	pressure, kPa
Pr	Prandtl number
Q_r	heat flux, $\text{J} \cdot \text{m}^{-2} \cdot \text{s}^{-1}$
r_0	catalyst particle radius, m
r_i	reaction rate of the i th step, $\text{mol} \cdot \text{kg}(\text{catalyst})^{-1} \cdot \text{h}^{-1}$
R	ideal gas constant, $\text{kJ} \cdot \text{kmol} \cdot \text{K}^{-1}$
Re	Reynolds number
Re_i	Reynolds number of the i th component
R_i	reaction rate, $\text{kg} \cdot \text{m}^{-3} \cdot \text{s}^{-1}$
Sh_i	Sherwood number of the i th component
S_c	Schmidt number
\bar{S}_i	mass source of the i th component of single model, $\text{kg} \cdot \text{m}^{-3} \cdot \text{s}^{-1}$
S	heat source of single model, $\text{J} \cdot \text{m}^{-3} \cdot \text{s}^{-1}$
s	surface conditions
\bar{S}	source term for the momentum equation, $\text{kg} \cdot \text{m}^{-3} \cdot \text{s}^{-1}$
S_f^h	fluid enthalpy source term, $\text{J} \cdot \text{m}^{-3} \cdot \text{s}^{-1}$
T	temperature, K
T^s	temperature at particle outer surface, K
u	apparent gas velocity, $\text{m} \cdot \text{s}^{-1}$
\vec{v}	gas velocity vector, $\text{m} \cdot \text{s}^{-1}$
\vec{v}^T	transpose of velocity vector, $\text{m} \cdot \text{s}^{-1}$

$\nu'_{i,r}$	stoichiometric coefficient for reactant i in the r th reaction
$\nu''_{i,r}$	stoichiometric coefficient for product i in the r th reaction
$\eta'_{i,r}$	rate exponent for reactant species j in the r th reaction
$\eta''_{i,r}$	rate exponent for product species j in the r th reaction
v_r^s	gas velocity at particle outer surface, $\text{m} \cdot \text{s}^{-1}$
Y_i	mass fraction of the i th component
Y_i^s	mass fraction of the i th component at the particle outer surface
$Y_{i,0}$	mass fraction of the i th component at bulk
ε	catalyst porosity
ρ_g	mixture gas density, $\text{kg} \cdot \text{m}^{-3}$
ρ_0	mixture fluid density at bulk, $\text{kg} \cdot \text{m}^{-3}$
ρ_{cat}	real catalyst density, $\text{kg} \cdot \text{m}^{-3}$
ρ_i	the i th component density, $\text{kg} \cdot \text{m}^{-3}$
μ	mixture fluid viscosity, $\text{Pa} \cdot \text{s}^{-1}$
$(\sum_{\nu})_i$	diffusion volume of the i th component, $\text{cm}^3 \cdot \text{mol}^{-1}$
λ	thermal conductivity, $\text{W} \cdot \text{s}^{-1} \cdot \text{K}^{-1}$
λ_i	thermal conductivity coefficient of the i th component, $\text{W} \cdot \text{s}^{-1} \cdot \text{K}^{-1}$
η	effectiveness factor of the i th step
ϕ	medium porosity
τ	curvature factor
$\bar{\tau}$	shear stress of gas phase, Pa
Nu_i	Nusselt number of the i th component

approach. Most of the early multi-scale modeling efforts in this field are practically multi-scale gas–solid two-phase FBRs [16]. Furthermore, to the best knowledge of our knowledge, no open report has been published regarding the development of a multi-scale CFD model for catalytic fixed-bed reactors.

Considered a typical example of a multi-scale fixed-bed reactor, the fixed-bed reactor for the oxidative dehydrogenation of butylene to butadiene (ODOBTB) is very important in the chemical industry [17]. Ferrite catalysts with high intraparticle pore volume and surface area are frequently used in the ODOBTB [18]. However, the majority of previous studies on ODOBTB over ferrite catalysts have focused on the oxidative dehydrogenation mechanism and kinetics. Few studies have examined the oxidative dehydrogenation reactors, particularly the multi-scale flow and reaction phenomenon in these reactors, which can be used to evaluate more accurately the reactor performance. Xiang et al. [19] developed a mathematical model for the dehydrogenation of butylene into butadiene in an FBR. Elementary and secondary reactions were incorporated in their model. Borio et al. [20] established a dynamic mathematical model for the dehydrogenation of butylene to butadiene in a fixed-bed reactor, which was used to optimize reactor operation conditions and improve the butadiene production rate. However, the catalyst intraparticle transfer was ignored in their work.

In this study, a multi-scale model is applied to describe the impacts of intraparticle transfer on the flow field and main composition distributions in a fixed-bed reactor for the ODOBTB over ferrite catalysts. This model uses a porous medium model coupled with a spherical porous pellet model and reaction kinetic model. Based on the multi-scale model, this simulation study

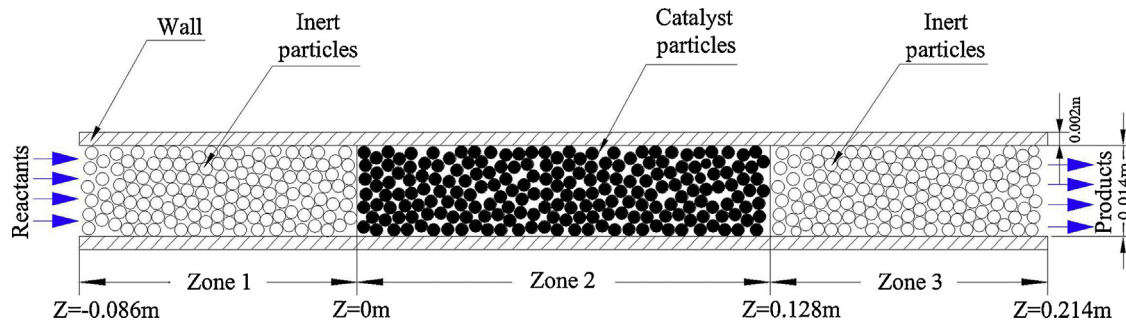


Fig. 1. Fixed-bed axial-flow reactor (reactants enter at $Z = -0.086$ m and leave at $Z = 0.214$ m. The reaction zone extends from $Z = 0$ m to $Z = 0.128$ m).

provides evidence to whether the intraparticle transfer limitation in fixed-bed reactors for the oxidative dehydrogenation over the ferrite catalysts can be generally ignored. Results from this study could give a novel understanding of fixed-bed reactors employed in the catalytic oxidative dehydrogenation reaction field.

Reactor and multi-scale model

Simulation reactor

A common fixed-bed reactor developed by Wu et al. [21] is chosen for the simulation (Fig. 1). The reactor, which has a length of 0.3 m and an inner diameter of 0.014 m, consists of three zones. Zone 1 preheats the reactants, and zone 3 cools the products after the heating. The gas reaction occurs in zone 2, which is located at the center of the reactor. Zones 1 and 3 are filled with inert particles, while zone 2 is filled with ferrite catalyst particles.

The multi-scale model

Given that the ODOBTA over ferrite catalysts is a typical gas–solid reaction system, these reactions normally occur at the active sites within catalyst particles. According to the Mars–van Krevelen mechanism, the reactants should diffuse through the gas boundary layer around the catalyst particles and subsequently through their pores to reach the active sites where the reactants are adsorbed and react [18]. By contrast, the products initially diffuse outwards through the catalyst surface active sites, subsequently through the catalyst matrix, and finally transported to the gas stream [18]. Therefore, the reactants and products should undergo the same process of intraparticle diffusion. Whether the effect of intraparticle diffusion resistance in the reaction can be ignored is unknown. Therefore, a multi-scale model that not only presents the fluid dynamic behavior but also describes the diffusion phenomenon within catalyst particles is necessary to simulate accurately the ODOBTA process in a fixed-bed reactor.

In this study, a multi-scale model was constructed by coupling a porous medium model (PMM) with an SPM. The PMM is used to describe the gas–solid flow in the fixed-bed reactor, and the SPM is used to represent the intraparticle transfer and reaction. These models are briefly summarized in Tables 1 and 2 [22–28]. The average gas velocity is approximately 0.033 m/s in the porous medium, and the numerical Re number is close to 6. Considering that Re is less than 10 in the fixed-bed reactor, the fluid flow is laminar flow [35], and the diffusion resistance at the exterior of the particles should be computed [Eqs. (18)–(26)]. In addition, the turbulence model need not be considered in the laminar flow.

The kinetics model adopted is presented as follows. Based on John et al. [30] and Ding et al. [29], the products of the reaction are butadiene, carbon dioxide, and vapor. Therefore, they inferred that

the main reaction steps are as follows:



Table 1

Main governing equations of the single particle model.

- (1) Continuity : $\epsilon \frac{\partial \rho_g}{\partial t} + \frac{v_r^2}{r^2} \frac{\partial}{\partial r} (r^2 \rho_g) = 0$
- (2) Species mass balance : $\epsilon \frac{\partial}{\partial t} (\rho_g Y_i) + \frac{v_r^2}{r^2} \frac{\partial}{\partial r} (r^2 \rho_g Y_i) = -\frac{1}{r^2} \frac{\partial}{\partial r} (r^2 j_{i,r}) + \xi_i$
- (3) Heat balance : $\left((1 - \epsilon) C_{p,cat} \rho_{cat} + \epsilon \rho_g \sum_{i=1}^n Y_i C_{p,i} \right) \frac{\partial T}{\partial t} = -\rho_g \sum_{i=1}^n Y_i C_{p,i} v_r^2 \frac{\partial T}{\partial r} - \frac{1}{r^2} \frac{\partial}{\partial r} (r^2 Q_r) + \hat{S}$
- (4) Ideal gas law : $\rho_g = \frac{pM}{RT}$
- (5) Definitions : $\sum_{i=1}^n Y_i = 1$
- (6) Darcy's law : $v_r = -\frac{BR}{\mu} \frac{\partial p}{\partial r} \Big|_s$
where
- (7) $B = \frac{\epsilon d_p^2}{32\tau}$
- (8) Heat flux : $Q_r = -\lambda \frac{\partial T}{\partial r}$
- (9) Mass source term : $\hat{S}_i = (1 - \epsilon) M_i \rho_{cat} r_i$
- (10) Heat source term : $\hat{S} = \sum (-\Delta H_{r_k}) \cdot r_k$
- (11) Diffusion flux : $j_{i,r} = -\rho_i D_{i,eff} \frac{\partial Y_i}{\partial r}$
- (12) where $D_{i,eff} = \frac{\epsilon}{\tau} \frac{1}{(1/D_{i,m}) + (1/D_{i,k})}$
- (13) where $D_{i,k} = 97 \frac{d_p}{2} \sqrt{\frac{T}{M_i}}$
- (14) $D_{i,m} = \frac{1 - Y_i}{M \sum_{j=1}^n \frac{1}{(Y_j/M_j D_{ij})}}$
 $j \neq i$
- (15) where $D_{ij} = \frac{0.00143 \times T^{1.75}}{PM_{ij}^{1/2} [(\sum_{\nu} \nu_i)^{1/3} + (\sum_{\nu} \nu_j)^{1/3}]^2}$

Boundary conditions:

- At $r = 0$:
- (16) $\frac{\partial Y_i}{\partial r} = 0$
 - (17) $\frac{\partial T}{\partial r} = 0$
- At $r = d_p/2$:
- (18) $k_{i,g} (Y_i^s - Y_i^f) = -Y_i^s D_{im} \frac{\partial Y_i}{\partial r} \Big|_s - v_r^s \rho_g Y_i^s$
 - (19) $\lambda \frac{\partial T}{\partial r} \Big|_s - \rho_g C_{p,cat} T^s v_r^s = h_{i,g} (T^f - T^s)$
where
 - (20) $k_{i,g} = \frac{D_{i,g} Sh_i}{d_p}$
 - (21) $Sh_i = 2 + 0.6 Sc_i^{1/3} Re_i^{0.5}$
 - (22) $Sc_i = \frac{\mu_i}{\rho_i D_{im}}$
 - (23) $Re_i = \frac{d_p u \rho_i}{\mu_i}$
 - (24) $h_{i,g} = \frac{k_{i,g} Nu_i}{d_p}$
 - (25) $Nu_i = 2 + 0.6 Pr^{1/3} Re_i^{0.5}$
 - (26) $Pr = \frac{c_{p,i} \mu_i}{\lambda_i}$

Table 2
Main governing equations of the porous medium model.

(27) Gas phase continuity equation :	$\frac{\partial(\phi\rho_g)}{\partial t} + \nabla \cdot (\phi\rho_g\vec{v}) = 0$
(28) Gas phase momentum equation :	$\frac{\partial(\phi\rho_g\vec{v})}{\partial t} + \nabla \cdot (\phi\rho_g\vec{v}\vec{v}) = -\phi\nabla p + \nabla \cdot \phi\vec{\tau} + \phi\rho_g\vec{g} + \vec{S}$
(29) Gas phase equation of state :	$p = \rho_g RT/M$
(30) Gas phase stress–strain tensor :	$\vec{\tau} = \mu[(\nabla\vec{v} + \nabla\vec{v}^T) - \frac{2}{3}\nabla \cdot \vec{v}\vec{I}]$
(31) Gas–solid momentum exchange rate :	$\vec{S} = 150 \frac{(1-\phi)^2 \mu}{d_p^2} \vec{v} + 1.75 \frac{\rho_g(1-\phi)}{d_p \phi} \vec{v} \vec{v}$
(32) Species conservation equation :	$\frac{\partial(\phi\rho_g Y_i)}{\partial t} + \nabla \cdot (\phi\rho_g \vec{v} Y_i) = -\phi\nabla \cdot \vec{J}_i + \phi R_i, i \in [1, N_r]$
(33) where	$\vec{J}_i = -\rho_g D_{i,m} \cdot \nabla Y_i$
(34) Mass rate of reaction :	$R_i = M_i \sum_{r=1}^{N_r} \left[(v'_{ir} - v''_{ir}) (k_{f,r} \prod_{j=1}^{N_r} [C_{j,r}]^{\alpha'_{j,r} + \eta'_{j,r}}) \right]$
(35) Energy equation :	$\frac{\partial(\phi\rho_g E_g + (1-\phi)\rho_{cat} E_s)}{\partial t} + \nabla \cdot (\vec{v}(\rho_g E_g + p)) = \nabla \cdot [k_{eff} \nabla T - (\sum_{i=1}^{N_r} h_i \vec{J}_i)] + \vec{\tau} \cdot \vec{v} + S_f$
where	
(36)	$k_{eff} = \phi k_g + (1-\phi)k_s$

The deductive equations of Ding et al. [29] on the basis of Mars–van Krevelen mechanism were in accordance with the experimental data. Thus, the reaction kinetic model of Ding et al. is adopted in this study. Ding et al. [29] stated that the catalytic reaction occurs at the oxidation active site (L). Hence, they deduced the elementary reaction and the kinetic equations. The kinetic model is shown as follows:

$$r_1 = \frac{k_1 P_{C_4H_8} k_0 P_0}{(k_1 + k_2) P_{C_4H_8} + k_3 P_{C_4H_6} + k_0 P_0}, \quad (40)$$

$$r_2 = \frac{k_2 P_{C_4H_8} k_0 P_0}{(k_1 + k_2) P_{C_4H_8} + k_3 P_{C_4H_6} + k_0 P_0}, \quad (41)$$

$$r_3 = \frac{k_3 P_{C_4H_6} k_0 P_0}{(k_1 + k_2) P_{C_4H_8} + k_3 P_{C_4H_6} + k_0 P_0}, \quad (42)$$

Table 3
Kinetic parameters for kinetic model.

Parameter	Values
A_0 (mol·kg(catalyst) ⁻¹ ·h ⁻¹ ·Pa ⁻¹)	6210
A_1 (mol·kg(catalyst) ⁻¹ ·h ⁻¹ ·Pa ⁻¹)	21258
A_2 (mol·kg(catalyst) ⁻¹ ·h ⁻¹ ·Pa ⁻¹)	79,993
A_3 (mol·kg(catalyst) ⁻¹ ·h ⁻¹ ·Pa ⁻¹)	81399
E_{a0} (kJ/mol)	-64.8
E_{a1} (kJ/mol)	-76.1
E_{a2} (kJ/mol)	-98.3
E_{a3} (kJ/mol)	-100

where

$$k_i = A_i \exp\left(\frac{E_{a_i}}{RT}\right). \quad (43)$$

Additionally, r_1 , r_2 , and r_3 represent the reaction rates of the chemical equations in Eqs. (37)–(39), respectively. More details on the kinetics parameters are listed in Table 3 [29].

Coupling mechanism of the multi-scale model

The coupling mechanism of the multi-scale model is shown in Fig. 2, which is explained by a four-step process.

Step 1: The temperature, mass fractions of species, and pressure distributions in the fixed-bed reactor are obtained after initialization. After the momentum balance and the continuity equations for the PMM [i.e., Eqs. (27)–(31)] are solved, each CFD numerical cell receives the information of the flow field.

Step 2: The temperature, mass fractions of species, and pressure distributions of each CFD numerical cell from Step 1 are forwarded to the SPM, which considers the variables as boundary conditions. Compared with a single numerical cell with the bulk of a fixed-bed reactor, the former is so small such that the parameter gradients within the cell can be neglected. Thus, the particles that belong to the one computational cell

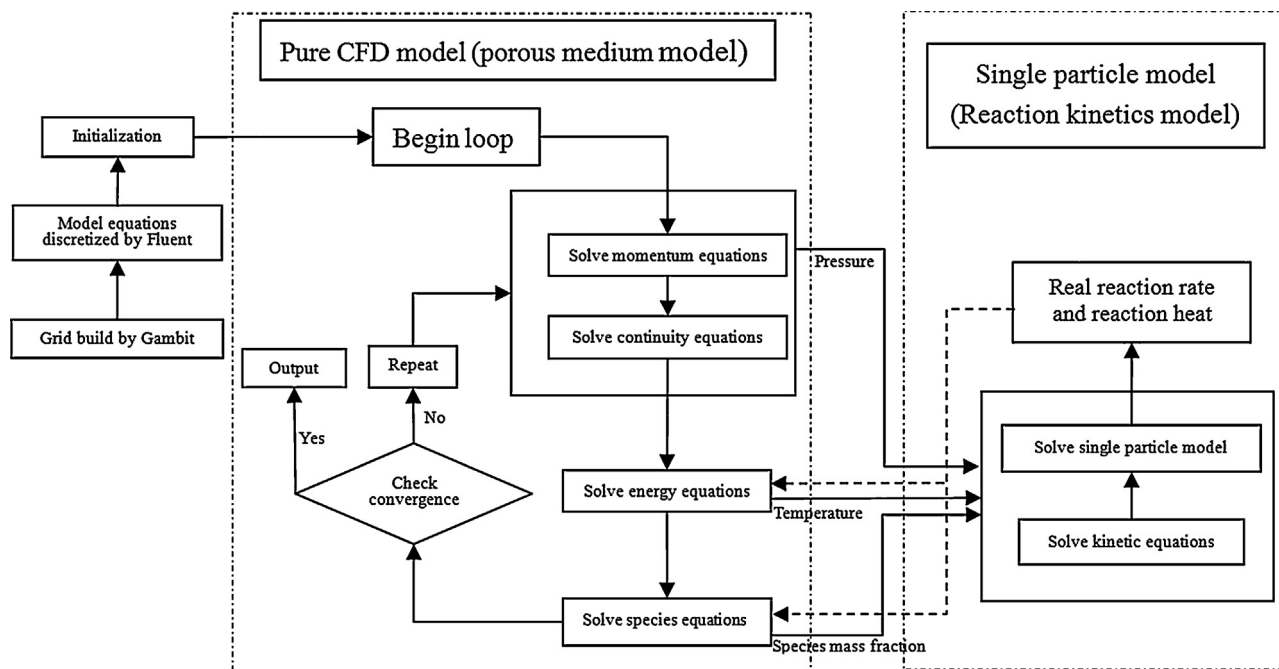


Fig. 2. The whole flow-sheet for solving the multi-scale model.

have similar boundary conditions. Finally, real reaction rates and heat are obtained by resolving the SMP [i.e., Eqs. (1)–(26)]. Step 3: The real heat and reaction rates are transmitted into the PMM, so that the CFD model obtains the source terms of the species transport equations and energy equations. These equations [Eqs. (32)–(36)] are solved to establish the temperature distributions and species mass fraction distributions. Step 4: The results are generated when the residuals of simulation meet the requirement. Thus, the precise flow field in the selected reactor is simulated, in which the influence of intraparticle transfer is considered.

Simulation conditions and modeling method

Model parameters

The simulation results depend on the series of parameters shown in Eqs. (1)–(36). The main boundary conditions and model parameters are shown in Table 4 [21,30–32]. Other parameters are presented in Tables 5 and 6 [33].

Modeling method

Based on the multi-scale model, two-dimensional simulations are performed with the commercial CFD code, FLUENT 6.3.26 (Ansys Inc., USA), in the double precision model. To simulate the two-dimensional fixed-bed reactor, the GAMBIT 2.3.16-a commercial grid-generation tool is used to generate the two-dimensional geometries and computational grids of the fixed-bed reactor. The

Table 4
 The parameters for the coupled model.

Descriptions	Value
Gas mixture	
$C_{p,g}$ mass heat capacity of gas ($\text{kJ} \cdot \text{kg}^{-1} \cdot \text{K}^{-1}$)	Mixing-law
ρ_g Gas density ($\text{kg} \cdot \text{m}^{-3}$)	Incompressible-ideal-gas
k_g Gas thermal conductivity ($\text{W} \cdot \text{m}^{-1} \cdot \text{K}^{-1}$)	Ideal-gas-mixing-law
$D_{i,m}$ Diffusion coefficient in CFD model ($\text{m}^2 \cdot \text{s}^{-1}$)	3.344×10^{-6}
μ Gas viscosity ($\text{Pa} \cdot \text{s}$)	Ideal-gas-mixing-law
Solid phase	
ϵ Intraparticle porosity	0.35
d_0 Intraparticle pore diameter (m)	1.55×10^{-8}
τ Particle curvature factor	4
ρ_{cat} Catalyst density ($\text{kg} \cdot \text{m}^{-3}$)	1919
$C_{p,cat}$ Catalyst heat capacity ($\text{J} \cdot \text{kg}^{-1} \cdot \text{m}^{-3}$)	1580
k_s Catalyst thermal conductivity ($\text{W} \cdot \text{m}^{-1} \cdot \text{K}^{-1}$)	0.2514
ω Permeability (m^2)	1.21×10^{-8}
C_2 Inertial resistance (m^{-1})	7586.1
Reactor parameters	
Inlet boundary condition	Velocity inlet
Outlet boundary condition	Pressure outlet
Wall boundary condition	No slip with 0.002 m
Wall thermal conditions	Constant temperature (611 K)
Operating pressure (Mpa)	0.1
Inlet gas velocity ($\text{m} \cdot \text{s}^{-1}$)	0.033
Inlet gas temperature (K)	611
Mole ratio of $\text{C}_4\text{H}_8:\text{O}_2:\text{H}_2\text{O}$	1:0.84:15
Transport and reaction	Volumetric reaction (By UDF)
Bed height (m)	0.3
Catalyst height (m)	0.128
ϕ Porosity	0.49
Bed diameter (m)	0.014
Particle diameter (mm)	2
Convergence criteria	10^{-3}

Table 5
 Mole heat capacity of species.

Component	$C_p^0/R = A + BT + CT^2 + DT^3 + ET^4 (\text{J} \cdot \text{mol}^{-1} \cdot \text{K}^{-1})$				
	A	$B \times 10^3$	$C \times 10^5$	$D \times 10^8$	$E \times 10^{11}$
C_4H_8	4.389	7.984	6.143	-8.197	3.165
C_4H_6	3.607	5.085	8.253	12.371	5.321
CO_2	3.259	1.356	1.502	-2.374	1.056
O_2	3.630	-1.794	0.658	-0.601	0.179
H_2O	4.395	-4.186	1.405	-1.564	0.632

governing equations in the PMM are discretized into a uniform structural grid via a finite volume method. First-order upwind method is used to discretize all terms in the PMM. Pressure and velocity are coupled via the SIMPLE algorithm. Moreover, the orthogonal collocation method coupled with the Newton method is used to solve the equations of the SPM. The SPM is incorporated into the PMM by user-defined functions. Sub-relaxation is used to ensure that the simulations converged. The grid independency analysis indicated that 4200 uniform cells are adequate to present the flow field in the selected reactor (Fig. 3).

Results and discussion

The flow field in zone 2 is shown because the reactions occur in this region.

Model validation

The experimental data from Wu et al. [21] are used to validate the multi-scale model. Table 7 shows that the simulated results from the multi-scale model agree well with the experimental data. Small relative errors are obtained for butylene and butadiene. The errors of carbon dioxide and oxygen are relatively large because the mass fractions of these two gases are small and close to the acceptable order of the error. However, the relative errors of carbon dioxide and oxygen, in which the intraparticle transfer limitation is ignored, are 6.3% and 39.8%, which exceed the tolerance of error. Furthermore, the accuracy of the multi-scale model is evaluated by the pressure drop in the fixed-bed reactor. The theoretical pressure drop is computed as 11.9 Pa using Eq. (44) [34,35].

$$\Delta p = 150 \frac{(1 - \epsilon)^2}{\epsilon^3} \frac{\mu_f u_0}{d_s^2} L. \quad (44)$$

The pressure drops simulated by the multi-scale model and the PMM coupling kinetic equations are 12.4 and 12.5 Pa, respectively. The pressure drops obtained from the different models again demonstrate that the multi-scale model is accurate and effective.

Reactor parameter distributions

Fig. 4 describes the parameter distributions related to work safety (i.e., temperature distribution) and production benefit (i.e., mass fraction distributions). The pressure drop is so small such that the fixed-bed reactor can be regarded as isobaric.

Table 6
 The physical property and mole enthalpy of species.

Component	M_i (kg/kmol)	Diffusion volume	$\Delta H_{f,298}$ (kJ/mol)
C_4H_8	56	77.7	-0.54
C_4H_6	54	73.0	110.00
CO_2	44	26.9	-393.51
O_2	32	16.3	-241.81
H_2O	18	13.1	0

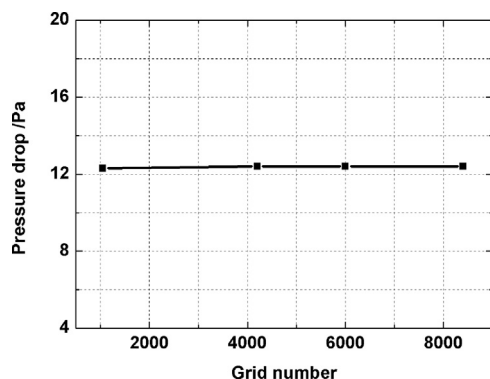


Fig. 3. Grid independency analysis.

Table 7

The comparison between simulated data and experiment data.

	Mass species fraction of main product at the outlet			
	C ₄ H ₆	C ₄ H ₈	O ₂	CO ₂
Pure CFD model coupling reaction kinetics model (grid: 4200)	0.135	0.0139	0.0162	0.0232
Coupled model (grid: 4200)	0.126	0.0237	0.0239	0.0180
Experiment	0.126	0.0231	0.0393	0.0229

Fig. 4(a) illustrates the temperature contour in the reactor. A hot spot exists in the reactor because the ODOBTB process is highly exothermic. The difference between the hot spot and its environment is not significant for reactants with low concentration. When the concentration of reactants is high, a temperature hot spot forms, which may be dangerous during production. Therefore, in the actual production, more heat should be removed around the entrance of the reactor for safety. Fig. 4(b)–(d) shows the mass fraction distributions of carbon dioxide, butylenes, and butadiene in the reactor, respectively. Butylene is the reactant, and its mass fraction gradually decreases along the axial direction. The concentration of the principal product butadiene varies greatly, while the by-product carbon dioxide presents little change in concentration.

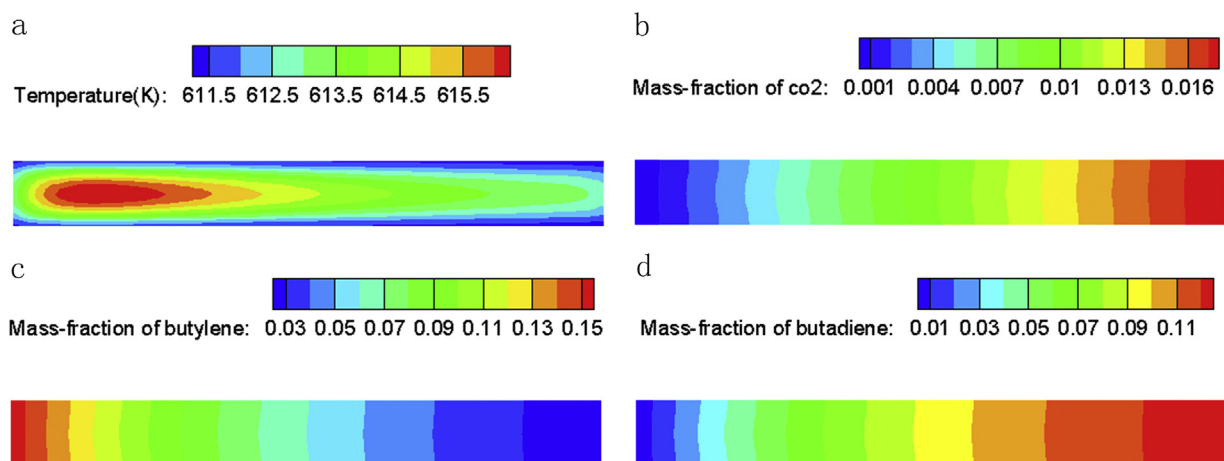


Fig. 4. The parameter distributions in the reactor ((a) the temperature contours, (b) the CO₂ distribution contours, (c) the butylene distribution contours, and (d) the butadiene distribution contours).

Intraparticle transfer

Herein, the PMM, which includes the kinetic equations, (*case 1*) and the multi-scale model (*case 2*) are used to investigate the intraparticle transfer phenomenon. The effectiveness factor is defined as the ratio of the actual reaction rate to the surface reaction rate of the particle. In previous modeling studies, the effectiveness factor was regarded as 1 when the surface reaction rate is 0 [14,16,28]. If the intrinsic reaction rate is zero, the reaction effectiveness factor is defined as 1 in this study.

Fig. 5 describes the temperature distributions of the two cases in the fixed-bed reactor. The bed temperature for *case 1* is lower than that for *case 2*, which is obvious especially at the hot spot. *Case 1*, in which the intraparticle transfer is ignored, has higher reaction rates than *case 2* [Fig. 6(a)], resulting in higher bed temperature. Thus, the simulated results for *case 1* deviate from the actual data, which can also be proved by the mass fractions of the main products at the reactor outlet. The mass fractions of butylene in *cases 1* and *2* are 0.014 and 0.0237, respectively, but the experimental result is 0.0237. Additionally, the length of the hot spot in *case 1* is longer than that in *case 2*, but the location of the hot spot in *case 2* is more accurate. Therefore, the temperature distribution, especially the hot spot, is closely related to the production benefit and safety when heat needs to be exchanged. In summary, intraparticle transfer phenomenon significantly affects the temperature of a fixed-bed reactor.

Fig. 7 shows the mass fraction distribution of butylene, butadiene, and carbon dioxide as well as the obvious difference between *cases 1* and *2*. In Fig. 7(a), the higher mass fraction of butylene for *case 2* indicates that the internal diffusion induces the decrease in the reaction rates of *steps 1* and *2* (Fig. 6). Given the intraparticle transfer limitation, the concentration of the reactant gradually decreases from the particle surface to the particle center [28]. Consequently, the concentration gradient within the catalyst particles reduces the average reaction rate, and the concentration of reactant for *case 2* is higher than that for *case 1*. Along the flow direction, the difference in the butylene mass fraction distributions in the two cases initially increases and then decreases. This phenomenon is referred to the self-stability described by Chen et al. [16]. The self-stability, namely, the interaction between the reactant concentration and the reaction rate, also exists in a fixed-bed reactor. Based on the difference in component mass fractions between the two cases, the fixed-bed reactor can be divided into three zones. Below 0.5 m bed height along the flow direction, the reactor is defined as the transport-controlled zone. At this zone, the

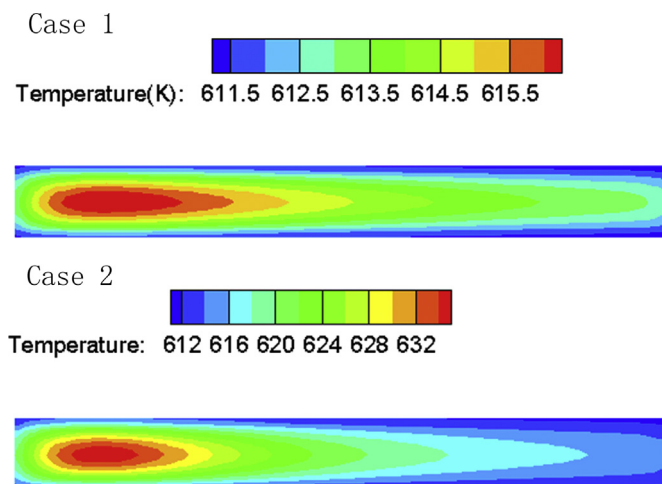


Fig. 5. The temperature distributions in the reactor (Case 1: the pure CFD model coupled with the reaction kinetic model and Case 2: the above validated coupled model).

difference in the butylene mass fractions between the two cases gradually increases as a result of the reduction in the reaction caused by the intraparticle transfer, consequently producing a higher fraction of reactant for *case 2*. Near to 0.5 m bed height, both reaction and diffusion are positive in the flow field, so this position is defined as the intermediate transition zone. Above 0.5 m bed height along the flow direction, the zone is defined as the reaction-controlled zone. At this zone, the positive influence of higher concentration of butylene exceeds the negative influence of the diffusion limitation within particles on the reaction rate, which reduces the gap of the butylene mass fractions between the two cases. The variation in the butylene reaction rate is observed from

Fig. 8(a). The reaction rate of butylene under *case 1* is greater than that under *case 2* at the transport-controlled zone, but they are equal at the intermediate transition zone. At the reaction-controlled zone, the reaction rate of butylene under *case 1* is lower than that under *case 2*. In other words, based on the butylene mass fractions, an obvious intraparticle mass transfer phenomenon exists for the ODOBTB system.

A significant impact of the intraparticle transfer limitation is verified by the difference in the butadiene mass fraction distributions between the two cases [**Fig. 7(b)**]. Similarly, the distinction of butadiene concentration in the two cases first increases and then decreases. In the transport-controlled zone, the limitation of intraparticle transfer decreases the reaction rate of butadiene, leading to lower butadiene mass fraction. With gas flowing along the flow direction, *case 2* has higher butylene and lower butadiene so the reaction rate at *Step 1* increases and that at *Step 3* decreases. Therefore, the difference in the butadiene mass fractions decreases in the reaction-controlled zone. The reaction rate variation is shown in **Fig. 8(b)**, which also explains the trend in the difference in the butadiene mass fraction distribution between the two cases.

An obvious difference in the carbon dioxide mass fractions between the two cases is observed in **Fig. 7(c)**, but the difference becomes increasingly larger. At the transport-controlled zone, the production rate of carbon dioxide is controlled by *Step 2* because the mass fraction of butylene is higher than that of butadiene. *Step 2* has a higher reaction rate under *case 1*, in which the model considers the diffusion limitation within particles. With height alteration, the production rate of carbon dioxide is controlled by *Step 3*, while the mass fraction of butylene is lower than that of butadiene, and then *Step 3* has a higher reaction rate under *case 1*. Therefore, the production rate of carbon dioxide under *case 2* is always smaller than that under *case 1* [**Fig. 8(c)**], which increases the difference in the carbon dioxide mass fractions. In summary,

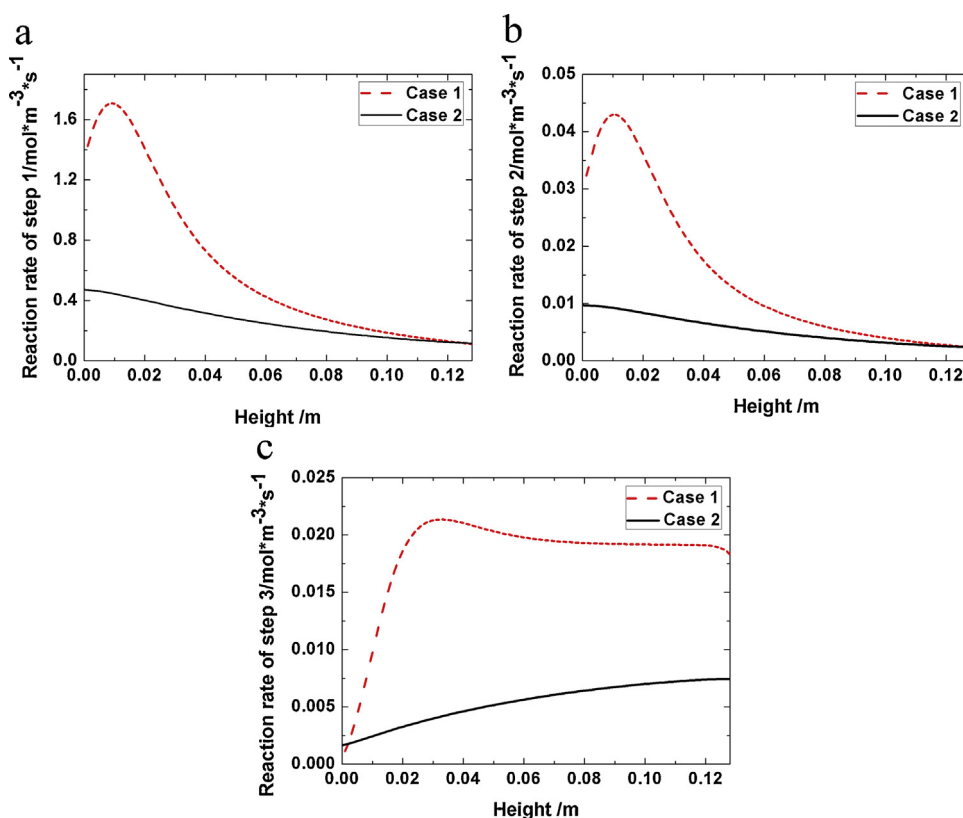


Fig. 6. Reaction step rates along the reactor height ((a) *Step 1*: r_1 , (b) *Step 2*: r_2 , and (c) *Step 3*: r_3).

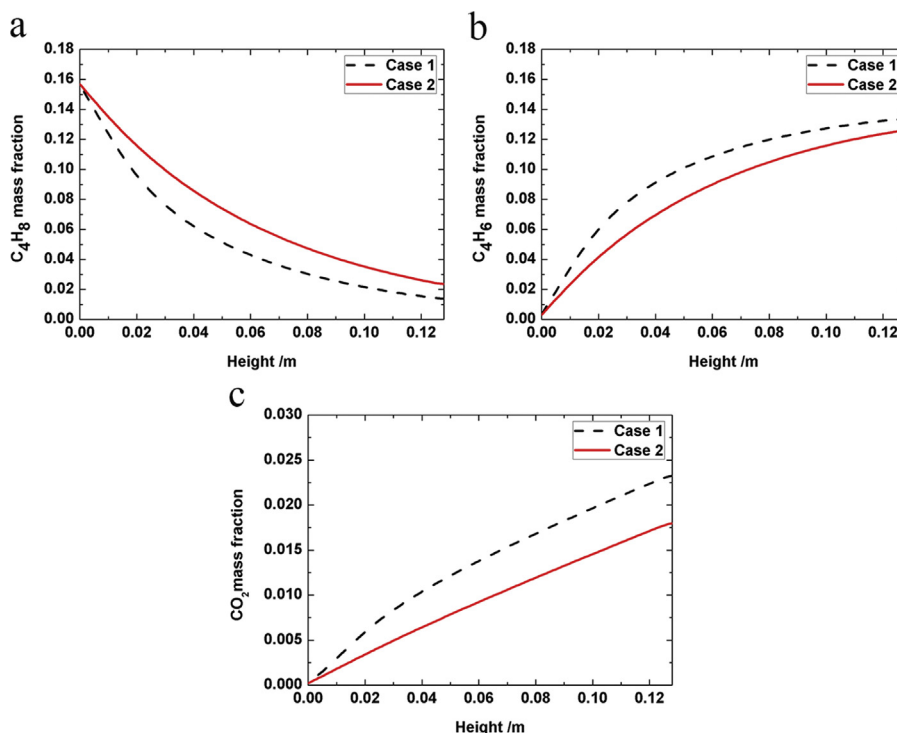


Fig. 7. Mass fraction of main species along the reactor height ((a) butylene, (b) butadiene, and (c) carbon dioxide).

based on the figures, observations and discussions, the intraparticle transfer phenomenon in a fixed-bed reactor cannot be ignored.

Fig. 9 illustrates the effectiveness factors of steps 1–3 at different heights. The effectiveness factor for steps 1 and 2 are approximately 0.954–0.959. The effectiveness factors for steps 1 and 2 are almost similar even if the activation energies of the two steps are different, which confirms that the temperature gradient within catalyst

particles can be neglected. In Fig. 9(a) and (b), the effectiveness factors for steps 1 and 2 gradually increase from the wall to 0.001 m distance and gradually decrease from 0.001 m to the center of the reactor where a minimum value appears. Based on the definition of the effectiveness factor, this trend is controlled by the mass fraction distributions of reactants because of the non-inclusion of the temperature gradient within the catalyst particles. Given the comparatively low temperature near the wall at the center of the

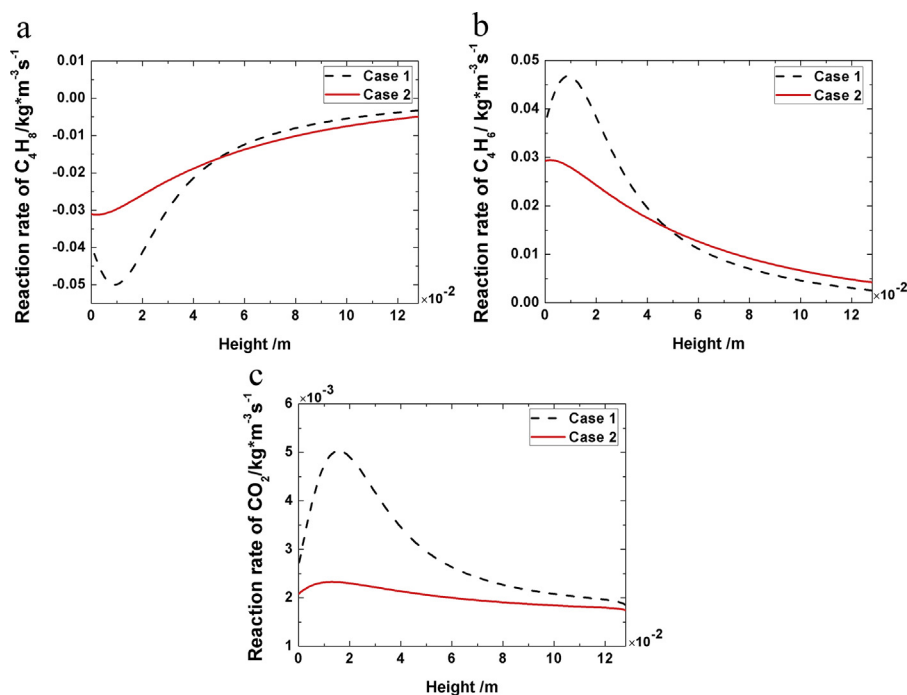


Fig. 8. Reaction rates of species along the reactor height ((a) butylene, (b) butadiene, and (c) carbon dioxide).

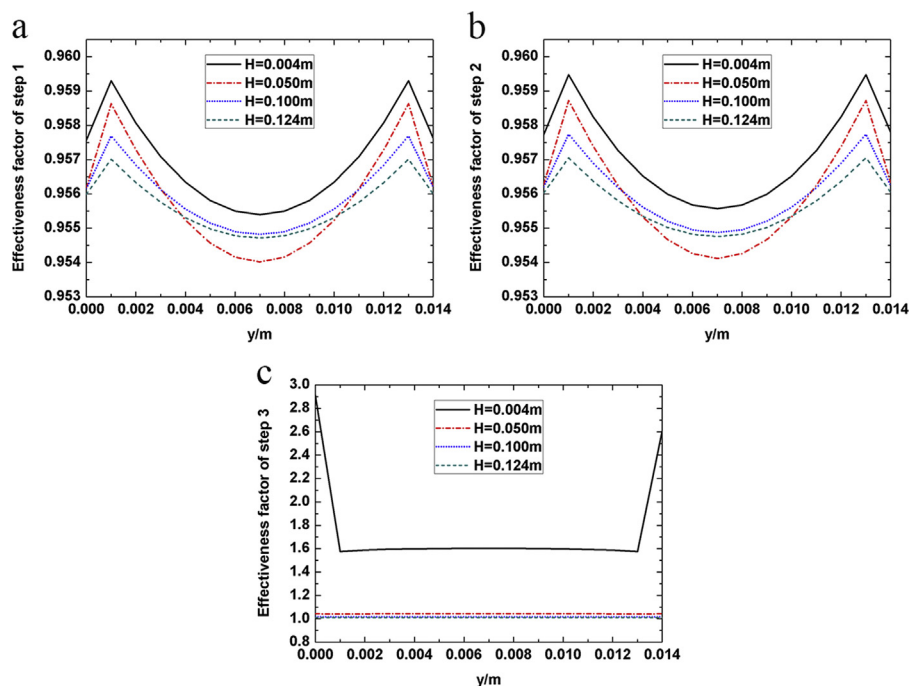


Fig. 9. Reaction step effectiveness factors at different reactor heights ((a) Step 1, (b) Step 2, and (c) Step 3).

fixed-bed reactor, the reaction is relatively low. When the fluid is away from the wall and the temperature gradually increases, the positive effect of temperature on the intraparticle transfer exceeds that on the reaction rate. This phenomenon weakens the concentration gradient within the catalyst particles. Thus, the effectiveness factor increases with distance from the wall. However, the closer to the center of reactor, the higher the temperature, which remarkably increases the reaction rate. At 0.001 m away from the wall of the reactor, the positive effect of temperature on the reaction rate exceeds that on the intraparticle transfer, which enhances the concentration gradient within the catalyst particles. Therefore, the effectiveness factor decreases as the center of reactor is approached. Consequently, the reverse trend of the effectiveness factor is observed in Fig. 9(a) and (b). In addition, at a height of 0.050 m, the effectiveness factor is minimized at the center of reactor because of the maximum temperature. The effectiveness factor of Step 3 is larger than 1 at a height of 0.004 m [Fig. 9(c)]. The reactant (butadiene) for Step 3 is the product of Step 1. The mass fraction of butadiene within the particle exceeds its concentration on the surface of the particle because of the limitation of intraparticle diffusion such that the effectiveness factor is larger than 1. With increased height, the mass fraction of butadiene considerably increases in the fluid such that the concentration gradient of butadiene within the particles can be ignored compared with the concentration of butadiene in the fluid. Thus, the effectiveness factor for Step 3 is approximately 1 at heights of 0.050, 0.100, and 0.124 m [Fig. 9(c)]. Accordingly, the effectiveness factor deviating from 1 proves the existence of intraparticle transfer phenomenon in the ODOBTF process. Moreover, the flow field, ODOBTF reaction, and the resistance interact in a fixed-bed reactor. Fig. 10 presents the effectiveness factor distributions in a fixed-bed reactor, and it is similar to the temperature distributions because a higher temperature results in a higher reaction rate. The trend of the effectiveness factor changes along the radial direction, which is consistent with above descriptions. Fig. 10 again demonstrates the existence of intraparticle transfer phenomenon in the ODOBTF process, so this phenomenon cannot be ignored.

Application of the multi-scale model

Four catalyst particle diameters ($d_p = 1.0, 1.5, 2.0,$ and 2.5 mm) are used to investigate the influence of diameter on the intraparticle transfer and flow field. Given that steps 1 and 2 have the same distributions, only the distribution of effectiveness factor for Step 1 is presented in the next sections. In Fig. 11(a), the effectiveness factor of Step 1 deviates from 1 with increased particle size, which indicates that a bigger particle size leads to greater intraparticle transfer limitation. The effectiveness factor is

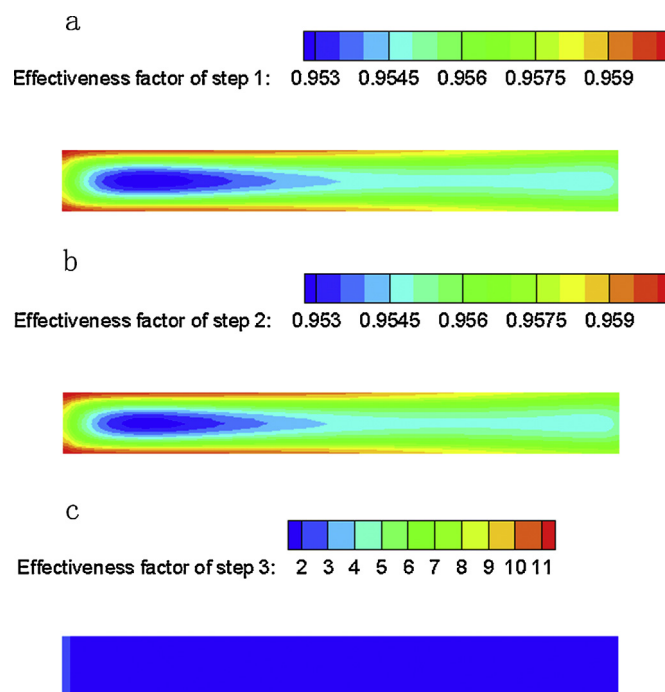


Fig. 10. Reaction effectiveness factor distributions in the reactor ((a) Step 1, (b) Step 2, and (c) Step 3).

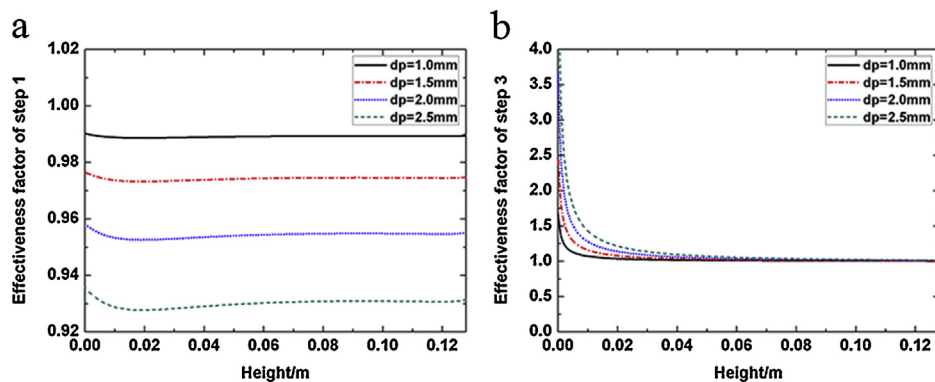


Fig. 11. The effectiveness factor distributions along the flow direction at different catalyst diameters ((a) Step 1 and (b) Step 3).

stable above 0.02 m height because the reaction rate and intraparticle diffusion are in equilibrium. In Fig. 11(b), with increased particle size, the effectiveness factor for Step 3 increases at the transport-controlled zone and is finally approximately 1, which is consistent to the description in the above section. In addition, the absolute difference in the butadiene mass fractions between the pure CFD model and the advanced model ($\Delta Y = Y_{\text{CFD}} - Y_{\text{coupled}}$) is shown in Fig. 12(a), which is important for profits. As described in the above section, the difference in all particle sizes first increases and then declines along the bed height direction. Fig. 12(b) illustrates the temperature distributions at the center of the reactor along the flow direction at different particle sizes. The small change in bed temperature reveals that the particle diameter slightly influences the bed temperature. Given the intraparticle transfer limitation, at the outlet, the butadiene mass fraction decreases when the catalyst particle diameter becomes larger [Fig. 12(c)].

Therefore, intraparticle transfer is important when the particle size increases, which can influence butadiene production. In a fixed-bed reactor, small particle diameter is advantageous to enhance butadiene production.

Fig. 13 describes the effectiveness factor distributions of steps 1 and 3 along the flow direction at four different space velocities, i.e., 240, 400, 516, and 636 h^{-1} . Space velocity has little effect on bed temperature under the lower reaction rate of Step 3. In Fig. 13(a), the effectiveness factors show similar trends at the inlet zone. At the transport-controlled zone, the effectiveness factor decreases with increased space velocity, while at the reaction-controlled zone, the factor increases with the space velocity. Considering that relatively lower reaction rates result in smaller concentration gradients within the catalyst particles, the effectiveness factors are similar under different space velocities at the inlet zone of the fixed-bed reactor. The increase in space velocity results in larger bed temperature [Fig. 14(b)]. When the fluid departs from the inlet

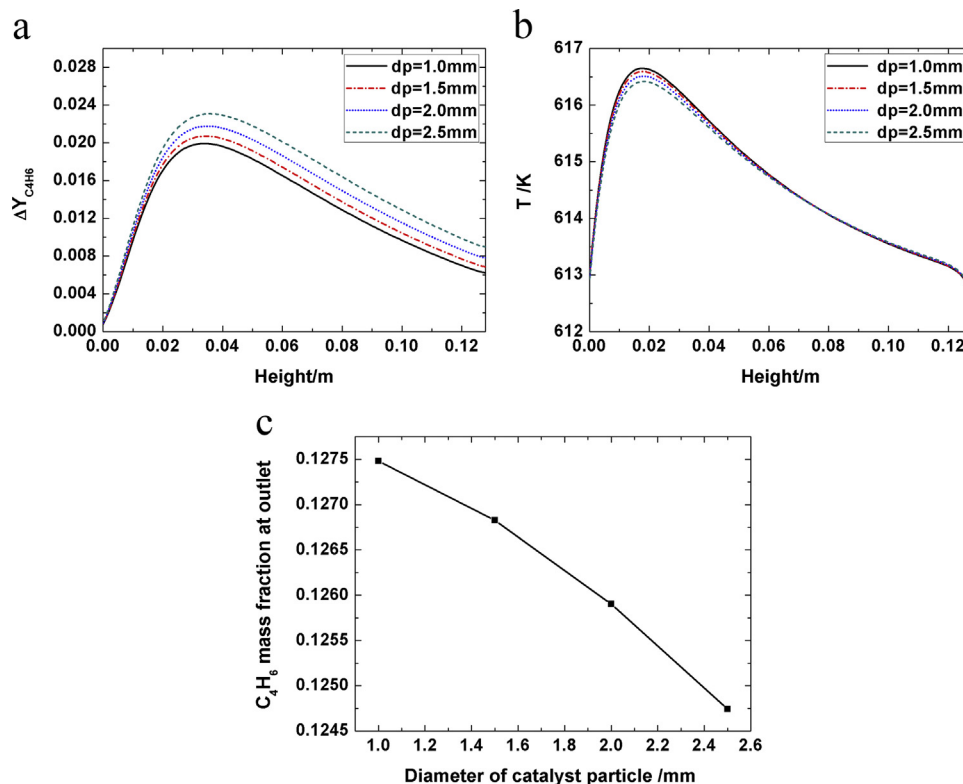


Fig. 12. (a) Distribution difference of butadiene along the flow direction between cases with and without the particle transfer limitation at different catalyst diameters, (b) temperature distribution along the flow direction at different catalyst diameters, and (c) butadiene mass fraction distribution under different catalyst diameters at outlet.

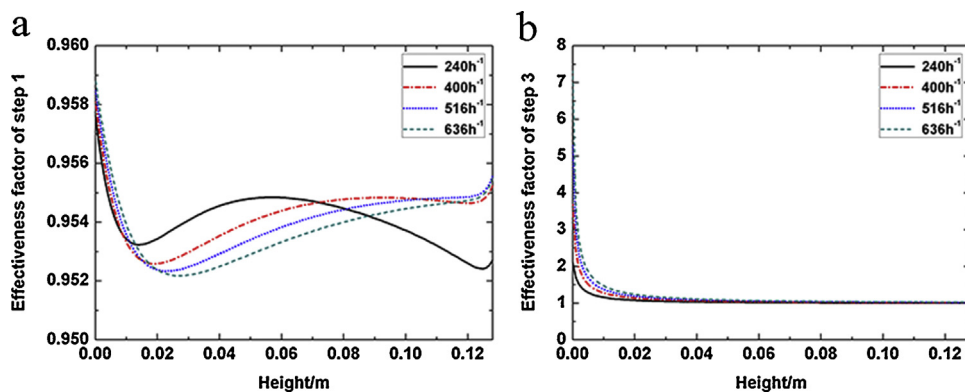


Fig. 13. The effectiveness factor distributions along the flow direction at different space velocities ((a) Step 1 and (b) Step 3).

zone, a higher temperature for the higher space velocity has a more significant effect on the reaction rate because of the relatively larger mass fraction of butylene. Therefore, the concentration gradient within catalyst particles in high space velocity is larger than that at low space velocity, leading to reduced effectiveness factors. At the reaction-controlled zone, a higher temperature has a more significant effect on the intraparticle transfer because of the higher space velocity and relatively lower mass fraction of butylene. Thus, the concentration gradient within the catalyst particles at high space velocity is lower than that at low space velocity, resulting in increased effectiveness factors. Fig. 14 illustrates the distributions of the absolute difference and bed temperature at the center along the flow field. In Fig. 14(a), when the space velocity is enhanced, the absolute difference hardly changes between 0 m and 0.040 m height and increases from 0.040 m to 0.128 m height. The variation in the absolute difference is that the residence time is shorter when the space velocity

increases. The space velocity raises the bed temperature along the flow direction. At the same height, the mass fraction of the reactants at high space velocity is larger than those at low space velocity, such that at high space velocity, the reaction generates more heat, which raises the bed temperature. The butadiene mass fraction decreases with space velocity [Fig. 14(c)]. Although a higher space velocity weakens the intraparticle transfer limitation, it also reduces the conversion of butadiene. To improve the reactor performance, the most appropriate space velocity should be chosen rather than increasing it.

Fig. 15 shows the change in the effectiveness factors of steps 1 and 3 along the flow direction at different wall temperatures, i.e., 608, 609, 610, and 611 K. In Fig. 15(a), the effectiveness factors decline with increased wall temperature, which indicates that the intraparticle transfer limitation of Step 1 attenuates as the higher wall temperature induces the increase in the concentration gradient of reactants within catalyst particles. In Fig. 15(b), the

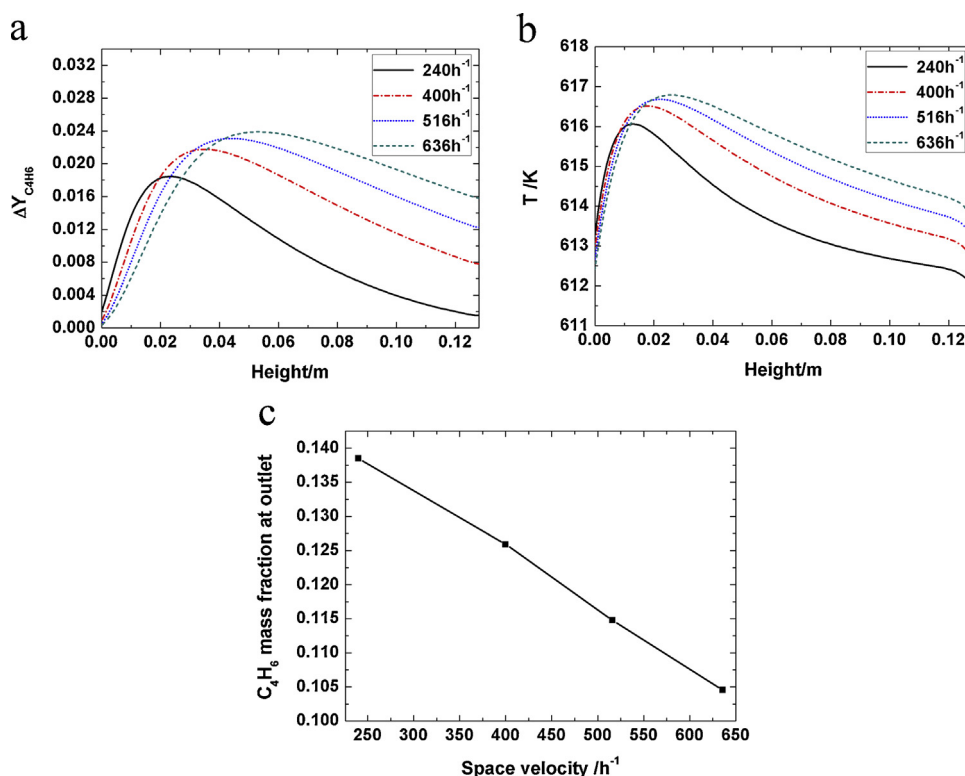


Fig. 14. (a) Distribution difference of butadiene along the flow direction between cases with and without the particle transfer limitation at different space velocities, (b) temperature distribution along the flow direction at different space velocities, and (c) butadiene mass fraction distribution under different space velocities at outlet.

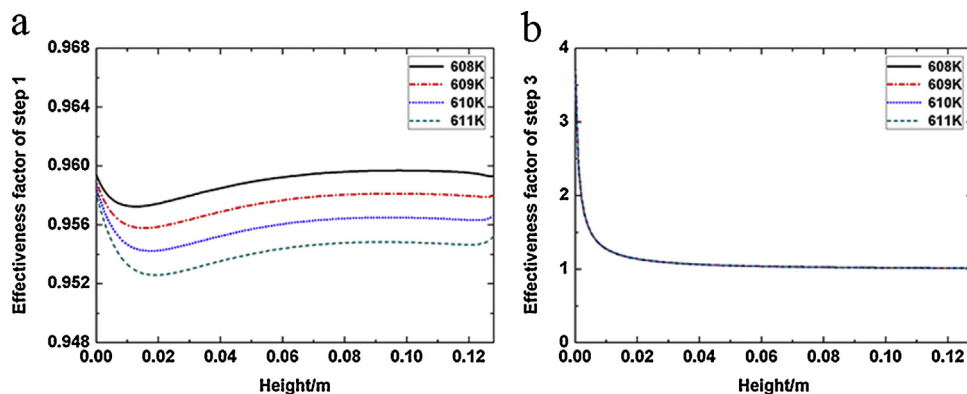


Fig. 15. The effectiveness factor distributions along the flow direction at different wall temperature ((a) Step 1 and (b) Step 3).

effectiveness factor of Step 3 is not related to the wall temperature. The activation energy of Step 3 is larger (Table 3) such that the wall temperature has little effect on its reaction rate, and then the effectiveness factor hardly changes with the increase in wall temperature. Fig. 16(a) describes the absolute difference distributions along the flow direction at different wall temperatures. The absolute difference initially increases and then drops with increased wall temperature. At the transport-controlled zone, given that a higher temperature causes the increase in concentration, the absolute difference in the high wall temperature is larger than that in low wall temperature. At the reaction-controlled zone, considering that the consumption of butylene for Step 1 at high wall temperature is faster than that at low wall temperature, the reaction rate of pure CFD model under high wall temperature decreases rapidly compared with that under low wall temperature. However, the reaction rate in the model coupled with the SPM

hardly changes. Thus, at the reaction-controlled zone, the reaction rate of Step 1 in pure CFD model is closer to the coupled model under high wall temperature (Fig. 17), resulting in decreased absolute difference. The bed temperature increases with the wall temperature [Fig. 16(b)]. The higher reaction rate is due to the larger wall temperature, which results in larger bed temperature. Moreover, Fig. 16(c) illustrates the variation in the butadiene mass fractions under different wall temperatures at the outlet. The conversion of butadiene increases with the wall temperature. In summary, although a higher wall temperature decreases the effectiveness factors, it decreases the difference in the mass fractions of butadiene between the two models at the reaction-controlled zone. In addition, the higher the wall temperature, the greater the bed temperature, which results in higher production. Therefore, changing the wall temperature is also an effective technique to improve production and optimize a reactor on the

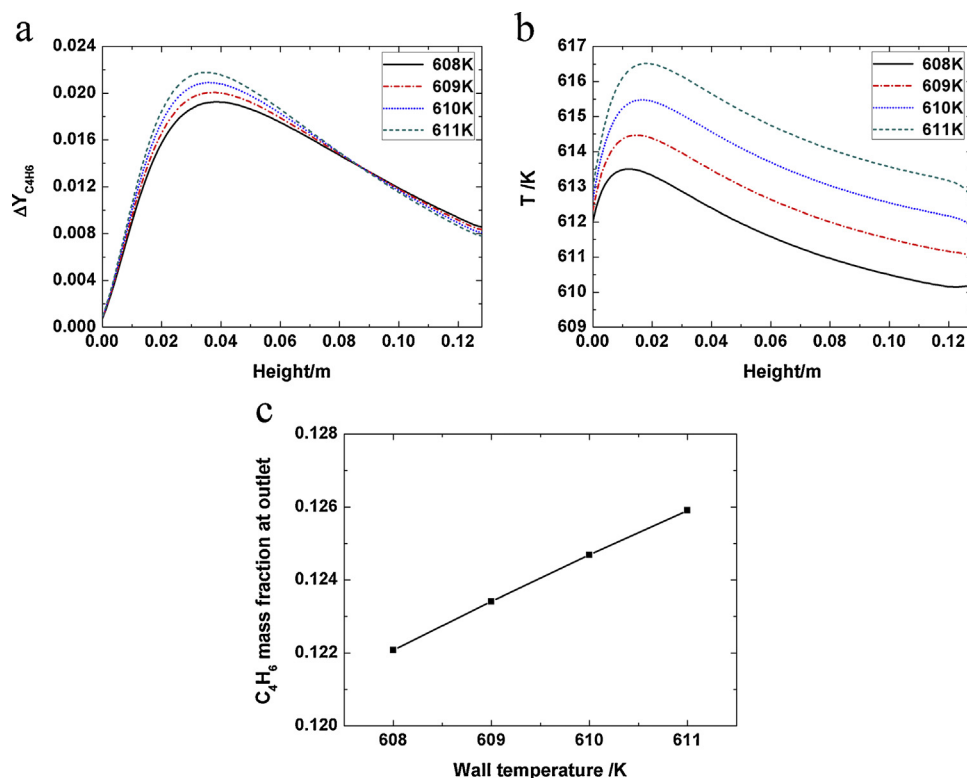


Fig. 16. (a) Distribution difference of butadiene along the flow direction between cases with and without the particle transfer limitation at different wall temperature, (b) temperature distribution along the flow direction between cases at different wall temperature, and (c) butadiene mass fraction distribution under different space velocities at outlet.

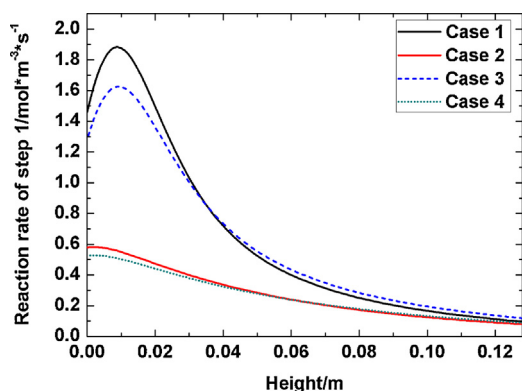


Fig. 17. Reaction rates along the reactor height (Case 1, Case 3: the pure CFD model coupling reaction kinetics at 613 K bed temperature, 610 K; Case 2, Case 4: the coupled model at 613 K, 610 K bed temperature).

condition that the ability of the reactor material, safety problem, and benefit are considered.

Conclusions

The intraparticle transfer limitation in fixed-bed reactors for the oxidative dehydrogenation over ferrite catalysts was thoroughly investigated numerically via a multi-scale model. The multi-scale model used a PMM and incorporated an SPM under the oxidative dehydrogenation condition. Based on the validated model and technology, a detailed study demonstrated the three typical oxidative dehydrogenation operating zones along the axial direction in a fixed-bed as a result of the self-stability of a fixed-bed reactor. The different operating zones were named as the transport-controlled, intermediate transition, and reaction-controlled zones, which were described in detail in this work. This study also demonstrated that the intraparticle transfer limitation was obvious and should not be ignored for the ODOBTD process in fixed-bed reactors. In addition, the flow field and parameter distributions were obtained by the advanced model, which are important for the safety of production and benefits of factory. The advanced model also determined the effect of operating conditions and parameters of the model on the flow field and the intraparticle transfer. Moreover, the influences of catalyst diameter, space velocity, and wall temperature on the butadiene mass fraction at the outlet of the reactor were discussed. The conversion of butadiene increased under higher wall temperature but declined when the space velocity and catalyst diameter were enhanced. Therefore, the results can be used to optimize a fixed-bed reactor, which is advantageous for a factory (i.e., for improving the yield of

butadiene and reducing energy consumption), and improve the safety of production (i.e., removal of the excess heat).

Acknowledgments

The authors thank the Fundamental Research Funds for the Central Universities (No. 2242014k10025), the National Ministry of Science and Technology of China (No. 2012CB21500402), the Research Fund for the Doctoral Program of Higher Education (No. 20130073110077), and the State-Key Laboratory of Chemical Engineering of Tsinghua University (No. SKL-ChE-10A03).

References

- [1] S.S. Cardoso, A.E. Rodrigues, *AIChE J.* 53 (2007) 1325–1336.
- [2] M. Saliccioli, M. Stamatakis, S. Caratzoulas, D.G. Vlachos, *Chem. Eng. Sci.* 66 (2011) 4319–4355.
- [3] J.H. Li, C.L. Cheng, Z.D. Zhang, J. Yuan, A. Nemet, F.N. Fett, *Chem. Eng. Sci.* 54 (1999) 5409–5425.
- [4] J.H. Li, J.Y. Zhang, W. Ge, X.H. Liu, *Chem. Eng. Sci.* 59 (2004) 1687–1700.
- [5] H.T. Bi, J.H. Li, *Adv. Powder Technol.* 15 (2004) 607–627.
- [6] W. Ge, F.G. Chen, J. Gao, S.Q. Gao, J. Huang, X.X. Liu, Q.C. Sun, L.M. Wang, W. Wang, *Chem. Eng. Sci.* 62 (2007) 3346–3377.
- [7] W. Wang, J.H. Li, *Chem. Eng. Sci.* 62 (2007) 208–231.
- [8] B. Lu, W. Wang, J.H. Li, X.H. Wang, S.Q. Gao, W.M. Lu, Y.H. Xu, L. Long, *Chem. Eng. Sci.* 62 (2007) 5487–5494.
- [9] B.L. Yang, X.W. Zhou, X.H. Yang, C. Chen, L.Y. Wang, *AIChE J.* 55 (2009) 2138–2149.
- [10] G. Dompazis, V. Kanellopoulos, V. Touloupides, C. Kiparissides, *Chem. Eng. Sci.* 63 (2008) 4735–4753.
- [11] R. Andersson, B. Andersson, F. Chopard, T. Noren, *Chem. Eng. Sci.* 59 (2004) 4911–4917.
- [12] J.H. Ghouse, T.A. Adams, *Int. J. Hydrogen Energy* 33 (2013) 9984–9999.
- [13] X.M. Chen, Z.H. Luo, Y.P. Zhu, J. Xiao, X.D. Chen, *Chem. Eng. Sci.* 104 (2013) 690–700.
- [14] Y.P. Zhu, G.Q. Chen, Z.H. Luo, *Ind. Eng. Chem. Res.* 53 (2014) 110–122.
- [15] A. Anca-Couce, N. Zobel, H.A. Jakobsen, *Fuel* 103 (2013) 773–782.
- [16] G.Q. Chen, Z.H. Luo, *Chem. Eng. Sci.* 109 (2014) 38–52.
- [17] A.G. Dixon, M. Nijemeisland, *Ind. Eng. Chem. Res.* 40 (2001) 5246–5254.
- [18] H. Lee, C.J. Jung, H. Kim, Y.M. Chung, T.J. Kim, S.J. Lee, S.H. Oh, Y.S. Kim, I.K. Song, *Catal. Lett.* 131 (2009) 344–349.
- [19] X.Z. Xiang, R.S. Zhu, *J. Qingdao Inst. Chem. Technol.* 21 (2000) 238–240.
- [20] D.O. Borio, N.S. Schbib, *Comput. Chem. Eng.* 19 (1995) 345–350.
- [21] X.G. Wu, H.Q. Liu, *J. Chem. Eng. Chin. Univ.* 9 (1995) 370–378.
- [22] Y.Q. Zhuang, X. Gao, Y.P. Zhu, Z.H. Luo, *Powder Technol.* 221 (2012) 419–430.
- [23] X.M. Chen, J. Dai, Z.H. Luo, *Particuology* 11 (2013) 703–714.
- [24] C.R. Wilke, *Chem. Eng. Prog.* 46 (1950) 95–104.
- [25] S. Vaishali, S. Roy, P.L. Mills, *Chem. Eng. Sci.* 63 (2008) 5107–5119.
- [26] K.R. Rout, J. Solsvik, A.K. Nayak, H.A. Jakobsen, *Chem. Eng. Sci.* 66 (2011) 4111–4126.
- [27] G.Q. Chen, Z.H. Luo, X.Y. Lan, C.M. Xu, J.S. Gao, *Chem. Eng. J.* 228 (2013) 352–365.
- [28] X.M. Chen, J. Xiao, Y.P. Zhu, Z.H. Luo, *Ind. Eng. Chem. Res.* 52 (2013) 3693–3707.
- [29] X.J. Ding, D.L. Xiao, X.L. Wang, S.L. Liu, *J. Mol. Catal.* 2 (1988) 25–30.
- [30] S.S. John, G.M. Howard, *ACS Pub.* 13 (1974) 54–58.
- [31] Y. Jin, Q.Q. Yu, X.Q. Xu, S. Wang, *Acta Sci. Nat. Univ. Pekin.* 3 (1986) 29–36.
- [32] Y. Jin, Q.Q. Yu, X.C. Hao, F.L. Yang, *J. Environ. Sci.* 7 (1986) 2–7.
- [33] E.P. Bruce, M.P. John, P. John, O'Connell, *The Properties of Gases and Liquids*, fifth ed., Chemical Industry Press, 2005.
- [34] S. Ergun, *Chem. Eng. Prog.* 48 (1952) 89–94.
- [35] B.C. Zhu, *Chemical Reaction Engineering*, fourth ed., Chemical Industrial Press, Beijing, 2011.